Journal of Power Sources 682 (2026) 240315

Contents lists available at ScienceDirect

Journal of Power Sources

journal homepage: www.elsevier.com/locate/jpowsour

High-performance polymer electrolytes with continuous fast-ion pathways for durable lithium metal batteries

Lehao Liu [a], Baoyi Wang [a], Mengxuan Zhang [a], Kunda Yang [a], Dingrong Long [a], Dongmei Zhang [a], Rubing Xu [a], Jiaxin Tu [a], Jiangping Zhang [a], Wei Lv [b], Shigang Ling [c], Jianan Gu [a], Lihua Chu [a], Bing Jiang [a], Qianxiao Fan [a], Ziyue Wen [a], Meicheng Li [a,*]

[a] State Key Laboratory of Alternate Electrical Power System with Renewable Energy Sources, School of New Energy, North China Electric Power University, Beijing, 102206, China
[b] Beijing Laboratory of New Energy Storage Technology, Institute of Energy Power Innovation, North China Electric Power University, Beijing, 102206, China
[c] Beijing Easpring Material Technology Co. Ltd., Beijing, 100160, China

HIGHLIGHTS

- Bridged LiIL@SiMS fillers create continuous fast-ion pathways in electrolyte.
- Room-temperature ionic conductivity of electrolyte increases by 17 times.
- Composite electrolyte shows superior dendrite inhibition ability for 6532 h.
- Composite electrolyte-based batteries display excellent cycling stability.

ARTICLE INFO

Keywords:
Polymer electrolyte
Silica particle
Ionic liquid
Lithium metal battery

ABSTRACT

Poly (ethylene oxide) (PEO)-based solid electrolytes with merits of flexibility, processability, and low cost provide avenues for augmented cell safety and superior energy density. However, they suffer from low room-temperature ionic conductivity, and inadequate mechanical strength, limiting their application in solid-state lithium metal batteries (LMBs). In this work, a Li^+-containing ionic liquid (LiIL)-functionalized silica molecular sieve (SiMS) (denoted as LiIL@SiMS) is developed as a multifunctional filler to modify PEO-based electrolytes. The confined LiILs within the SiMSs with interconnected "particle-to-particle bridging" networks work as continuous fast-ion transport pathways, dramatically increasing the ionic conductivity (2.54×10^{-4} vs. 1.41×10^{-5} S cm^{-1} at room temperature) and electrochemical oxidation stability potential (4.65 vs. 3.88 V) of electrolytes. Attributed to the three-dimensional (3D) continuous LiIL@SiMS distribution, the composite electrolyte also exhibits superior mechanical properties with tensile strength and Young's modulus reaching 2.17 and 19.11 MPa (vs. 0.60 and 0.21 MPa), respectively. Thus, the Li||Li symmetric cell assembled with the composite electrolyte demonstrates durable cycling life of 6532 h, while the composite electrolyte-based Li||$LiFePO_4$ cell also displays excellent cycling stability. This study establishes an "particle-to-particle bridging" conductive strategy for highly stable PEO electrolyte-based solid-state LMBs.

1. Introduction

The triad of attributes of superior energy density, exceptional cycling durability, and swift charging rates propels lithium-ion batteries into critical roles such as portable electronics, life-sustaining medical instruments, spacecraft power units, and modular energy storage packs [1–4]. However, commercial lithium batteries contain a large number of organic liquid electrolytes, which suffer from volatility, leakage, flammability, and explosion hazards [5–7]. Additionally, lithium dendrite growth during charging process can penetrate separators, causing internal short circuits and ignition. Replacing liquid electrolytes by solid-state electrolytes shows an important route to achieving high-safety and high-energy-density lithium metal batteries (LMBs) [8–12]. Compared with inorganic solid electrolytes, poly (ethylene

* Corresponding author.
E-mail address: mcli@ncepu.edu.cn (M. Li).

https://doi.org/10.1016/j.jpowsour.2026.240315
Received 18 January 2026; Received in revised form 3 April 2026; Accepted 4 May 2026
0378-7753/© 2026 Elsevier B.V. All rights are reserved, including those for text and data mining, AI training, and similar technologies.

oxide) (PEO)-based solid polymer electrolytes have obvious merits of straightforward synthesis, excellent film-forming characteristics, inherent flexibility, and conformal electrode/electrolyte interfacial contact, thus showing potential for mass production by using existing manufacturing infrastructure [13–16]. Nevertheless, their practical utilization in solid-state LMBs remains hindered by insufficient ionic conductivity at ambient temperature, deficient mechanical properties, and narrow voltage operation range [17–20].

Adding inorganic nanoparticles into polymer electrolytes would destroy the crystalline structure of polymers, and facilitate the polymer segment movement, which will greatly increase the ionic conductivity of polymer electrolytes [21–25]. Moreover, nanosized fillers have large specific surface area and the surface is modified with various Lewis acid groups [26,27]. According to Lewis acid-base theory, the adsorption of anions (of lithium salts) on the Lewis acidic sites facilitates lithium salt dissociation and enhances Li^+ transference numbers [28–30]. Nanofillers possessing elevated elastic modulus and thermal resistance can enhance both the mechanical robustness and thermal endurance of polymer electrolytes [17,31–34].

Silica-based molecular sieves (SiMSs) have abundant mesoporous structure, high specific surface area and rich functional groups on the surface, and thus are suitable as nanofillers for modifying polymer electrolytes [35–37]. However, the ionic conductivity of composite polymer electrolytes cannot be greatly enhanced, owing to poor ionic conductance and incontinuous distribution of the nanoparticles in the polymer matrices [38–41]. Apart from nanoparticle fillers, Li^+-containing ionic liquids (LiILs) are also considered as an important additive, because of their elevated thermal decomposition thresholds and high ionic conductivity, and solvation effect in polymer electrolytes [42,43]. Nevertheless, the incorporation of LiILs would compromise mechanical integrity and electrochemical stability of polymer electrolytes [44]. Thus, proper combination of SiMSs and LiILs with their advantages remains a challenge.

In this work, LiIL (i.e., 1-ethyl-3-methylimidazolium bis (trifluoromethylsulfonyl) imide, EMIMTFSI)-containing SiMSs (denoted as LiIL@SiMSs) are exploited as a multifunctional filler to improve the electrical, mechanical and electrochemical properties of PEO-based electrolytes (Fig. 1a). SiMSs (i.e., SiO_2 with amino functionalized groups) possess abundant pore structures (larger pore diameter of 3.419 nm than those (7.9 and 7.6 Å) of $EMIM^+$ and $TFSI^-$ ions [42]) and exceptional adsorption capacity, enabling the LiIL infiltration with the help of electrostatic interaction and capillary effect. Compared to the pristine PEO-lithium bis(trifluoromethane)sulfonimide (LiTFSI) electrolyte (denoted as PL), the confined LiILs within the bridging SiMS networks serve as continuous fast-ion transport pathways, greatly increasing the ionic conductance and mechanical strength of the polymer electrolyte (Fig. 1b). Furtherly, the confinement of LiILs in the SiMSs prevents the leakage of LiILs, broadening the electrochemical window of the PEO-LiTFSI-LiIL@SiMS composite electrolyte (denoted as PL-LiIL@SiMS). Consequently, the PL-LiIL@SiMS composite electrolyte demonstrates exceptional lithium dendrite resistance, enabling great improvement in LMBs cycling stability.

2. Experimental section

2.1. Preparation of LiIL@SiMSs

2 g dried LiTFSI (≥99%, Aladdin) was added in 2.73 g EMIMTFSI (99.9%, InnoChem), and then stirred at 40 °C until complete melting of LiTFSI to obtain LiILs. After that, LiILs and SiMSs (XFNANO) were mixed with different mass ratio (0.5:1, 1:1, 1.5:1, 2:1, 2.5:1 and 3:1), grinded with a mortar for 10 min (to ensure complete filling of LiILs in SiMSs), and treated at 80 °C for 12 h in vacuum to obtain LiIL@SiMSs.

2.2. Preparation of composite electrolytes

LiIL@SiMSs were added in 36 mL N, N-dimethylformamide (DMF) (>99.9%, InnoChem), ultrasonicated for 4 h, and then magnetically stirred for 4 h to obtain homogeneous LiIL@SiMS dispersions. LiTFSI (≥99%, Aladdin) and PEO (Sigma-Aldrich, Mw = 600,000) was then added in the LiIL@SiMS dispersions and stirred until complete dissolution to obtain PEO/LiTFSI/LiIL@SiMS mixture solutions. Total mass of LiIL@SiMSs, PEO, and LiTFSI was 2.5 g with an EO:Li^+ molar ratio of 18:1. The mixture solutions were poured into a PTFE mold and vacuum-dried at 60 °C for 72 h, peeled from the mold, and hot-pressed at 50 °C for 12 h to obtain the composite electrolyte membrane of PL-LiIL@SiMSx (x = 1, 5, 10, or 15). For comparison, the PEO-LiTFSI electrolytes containing SiMSs, LiILs, or LiILs and SiMSs were labeled as PL-SiMS, PL-LiIL, or PL-LiIL+SiMS, respectively. The electrolyte membranes were cut into circular discs of 19 mm in diameter using a slicer, and then kept in an argon-containing glove box (H_2O/O_2 < 0.1 ppm) for subsequent use.

2.3. Material characterizations

Microstructural characteristics of electrolytes and Li electrodes were examined via a Hitachi SU8010 field emission scanning electron microscope (SEM). A FEI F20 field emission transmission electron microscope (TEM) coupled with an energy-dispersive X-ray spectroscope (EDS) was utilized to characterize the microstructure of SiMSs and LiIL@SiMSs. The crystal structure of the electrolytes were characterized using a Bruker AXS D8 Focus X-ray diffractometer (XRD). Thermal be-

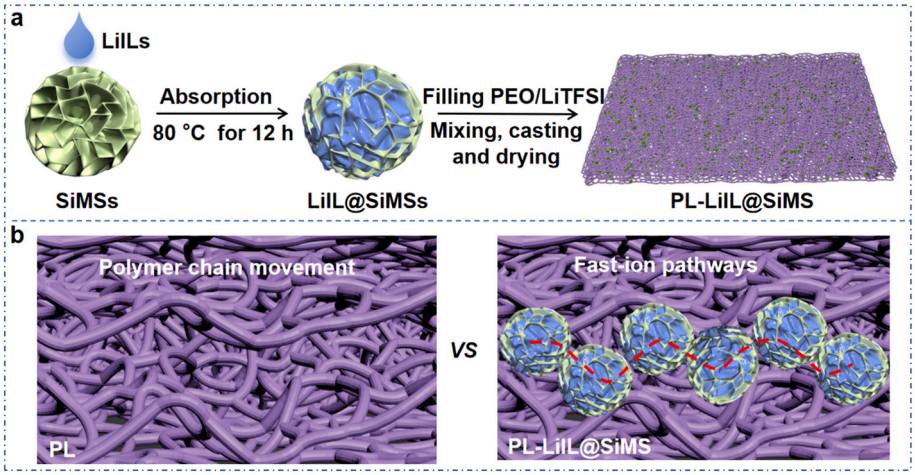


Fig. 1. Schematic descriptions of (a) preparation process of PL-LiIL@SiMS electrolyte and (b) ionic transport mechanism.

haviors were assessed by using a Hitachi STA7300 simultaneous thermogravimetry/differential thermal analyzer (TG/DTA) under nitrogen atmosphere. Crystallinity of the polymer electrolytes was determined by a DSC6000 differential scanning calorimeter (DSC). Crystallinity (χ_c) was calculated by using Equation (1):

$$\chi_c = (\Delta H/\chi \times \Delta H_{PEO}) \times 100\% \quad (1)$$

Where ΔH was the electrolyte enthalpy change, ΔH_{PEO} was the melting enthalpy of pure PEO (213.7 J g^{-1}), and χ was the mass fraction of PEO in the electrolyte. Full pore analysis of SiMSs before and after LiIL filling was conducted on a Quantachrome Autosorb IQ instrument with degassing condition set at 100 °C for 8 h. A constant strain rate of 2 mm min^{-1} was applied via a JB-126A universal testing machine to evaluate mechanical tensile properties of the electrolyte membranes.

2.4. Electrochemical measurements

The electrochemical impedance test was conducted on stainless steel (SS)||SS cells by using a Zahner electrochemical workstation in a frequency range of 1 M−10 mHz. The impedance spectra were fitted using a Zview software to obtain the required resistance values. The calculation formula for the ionic conductivity (σ) of the electrolytes was described as follows:

$$\sigma = \frac{L}{R \times A} \quad (2)$$

Where L denoted the thickness of the electrolytes, R denoted the electrolyte impedance, and A denoted the contact area between the electrolytes and the SS gaskets. Furthermore, the activation energy (E_a) was calculated according to the calculation formula as follows:

$$\sigma = \frac{A}{T} e^{-\frac{E_a}{R \times T}} \quad (3)$$

Where A denoted the pre-exponential factor, R is the ideal gas constant (8.314 J mol^{-1} K^{-1}), and T denoted the absolute temperature. Electrochemical stability windows of electrolytes were characterized via linear sweep voltammetry (LSV) by using a CHI660E electrochemical workstation with a scanning rate of 1 mV s^{-1}.

The critical current density (CCD) of Li||Li batteries was tested by using a Neware battery testing system. Cycling stability was evaluated at 0.1 mA cm^{-2} with 1 h stripping/plating steps at 60 °C. The $LiFePO_4$ (LFP) electrode consists of 80 wt% LFP active material, 10 wt% polyvinylidene fluoride binder, 9.7 wt% conductive carbon black and 0.3 wt % multi-walled carbon nanotubes as additional conductive additives. The active material loading was maintained at approximately 2.0 mg cm^{-2} for all cathodes. Solid-state Li||LFP cells were cycled at various current densities of 0.1, 0.2, 0.3, 0.5 and 1C within 2.5–3.8 V to determine the rate capability (1C = 170 mAh g^{-1}), and also cycled at 0.1C and 60 °C to determine the cycling stability. Solid-state Li||$LiNi_{0.6}Co_{0.2}Mn_{0.2}O_2$ cells were prepared with Li foil anodes and ~1.4 mg cm^{-2} $LiNi_{0.6}Co_{0.2}Mn_{0.2}O_2$-containing cathodes (MGL NEW MATERIALS) and cycled between 2.8 and 4.2 V at 30 °C using different C rates (1C = 180 mAh).

3. Results and discussion

3.1. Physicochemical properties of LiIL@SiMSs

SiMSs were mixed with LiILs with various mass ratios (0.5:1, 1:1, 1.5:1, 2:1, 2.5:1 and 3:1 of LiIL:SiMS) to prepare the LiIL@SiMS particles and then compressed for pellets (Fig. 2a–b). When the proportion of LiILs was relatively low, the appearance of SiMSs had no obvious change. However, when the LiIL:SiMS mass ratio increased to 2.5:1, the viscosity of the powders increased, and they were easy to agglomerate into small particles. Meanwhile, a large number of LiILs leaked on the LiIL@SiMS pellets. Thus, the LiIL:SiMS mass ratio should be lower than 2:1.

The effect of LiIL:SiMS mass ratio on the ionic conductivity of the LiIL@SiMS pellets was then investigated (Fig. 2c). As the LiIL content increased, the ionic conductivity of the LiIL@SiMS pellets gradually increased, because of fast-ion pathways in the pellets. At a LiIL:SiMS mass ratio of 2:1, the ionic conductivity increased to 1.67×10^{-3} S cm^{-1} at 30 °C. Further increase of the LiIL content yielded negligible improvement in the ionic conductivity, because of the pores were fully filled with LiILs. To maximize LiIL loading while avoiding leakage risks

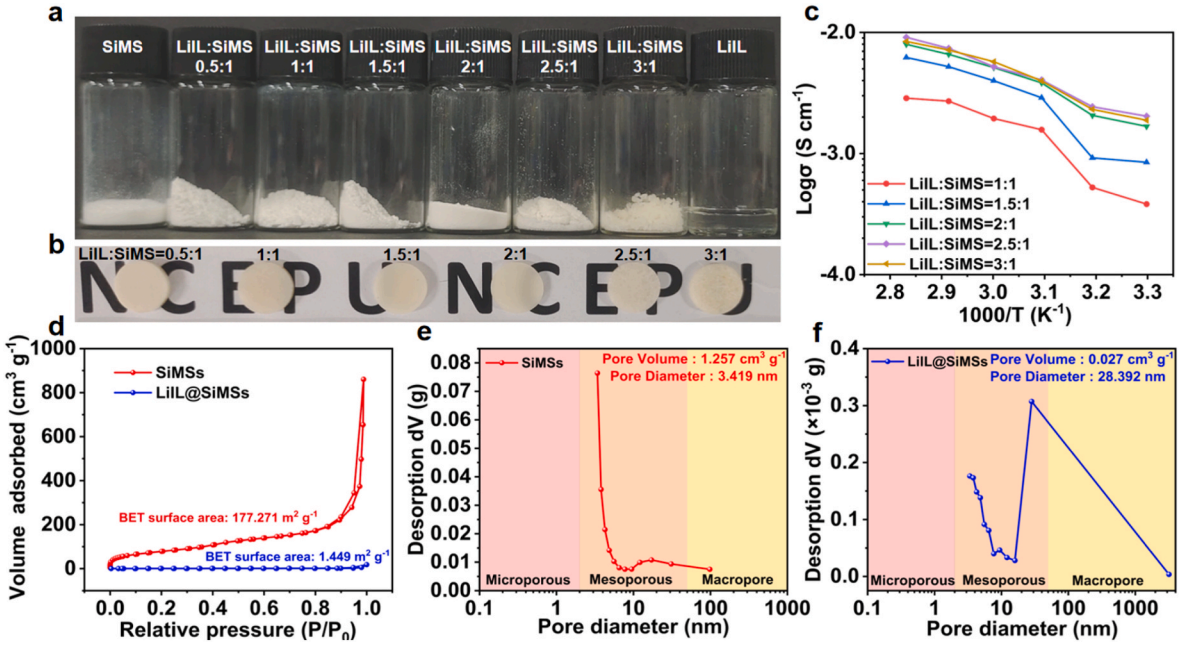


Fig. 2. (a) Optical photographs of LiIL@SiMSs with different weight ratios of LiIL to SiMS. (b) Optical photographs of LiIL@SiMS pellets with different weight ratios of LiIL to SiMS. (c) Ionic conductivity of LiIL@SiMS pellets at various temperatures. (d) N_2 adsorption-desorption isotherms of SiMSs and LiIL@SiMSs. Pore size distributions of (e) SiMSs and (f) LiIL@SiMSs.

(and nanoparticle aggregation), the LiIL:SiMS mass ratio of 2:1 was selected for subsequent studies.

The microstructure of the SiMSs before and after the LiIL filling was also studied. TEM characterizations revealed that the LiIL@SiMSs still remained the chained structure with "particle-to-particle bridging", which would be beneficial for facilitating the ion transport (Fig. S1 and S2). The EDS mappings of Si, O, S, N, and F elements confirmed the effective filling of LiILs in the SiMSs. The resultant isotherms and full pore analysis measurements further proved that the pristine SiMSs had an average pore diameter of 3.419 nm and large specific surface area of 177.271 $m^2 g^{-1}$ and pore volume of 1.257 $cm^3 g^{-1}$ (Fig. 2d–f). However, after the filling of LiILs to form the LiIL@SiMSs, the specific surface area drastically decreased to 1.449 $m^2 g^{-1}$, and the pore volume dropped to 0.027 $cm^3 g^{-1}$. This further confirmed that the LiILs were successfully filled in the pores of the SiMSs. Because of the filling of LiILs in the pores of the SiMSs and the formation of large voids between the aggregated LiIL@SiMSs, the pore diameter increased from 3.419 nm to 28.392 nm.

3.2. Morphology of electrolytes

The LiIL@SiMSs were incorporated in PEO-LiTFSI electrolytes for preparing PL-LiIL@SiMS composite electrolytes with various LiIL@SiMS content of 0–20 wt% (Fig. S3), and their ionic conductivities were measured at different temperatures (Fig. S4). The ionic conductivity of the electrolytes progressively increased with the LiIL@SiMS content, due to the increase of the fast-ion transport channels. The ionic conductivity of the composite electrolytes increased from 5.88 × 10^{-5} to 2.54 × 10^{-4} S cm^{-1} at 30 °C, when the LiIL@SiMS content increased from 5 to 15 wt%. Because of the severe deformation of the electrolyte with 20 wt% LiIL@SiMS loading, the optimal LiIL@SiMS loading for the composite electrolyte was selected to be 15 wt%. Apart from the composite electrolyte with 15 wt% LiIL@SiMSs (denoted as PL-LiIL@SiMS in the following sections), the PL electrolytes with 5 wt% SiMSs (denoted as PL-SiMS), 10 wt% LiILs (denoted as PL-LiIL), and 5 wt% SiMSs and 10 wt% LiILs (denoted as PL-LiIL+SiMS) were also prepared as control samples.

As shown in Fig. 3, the PL electrolyte has a rough surface. There are many pores in the PL-LiIL and PL-LiIL+SiMS electrolytes (indicated by white circles), which should be attributed to the incorporation of the LiILs (evaporation during the electrolyte desiccation process). Similar to the PL-SiMS electrolyte, there are no visible pores in the PL-LiIL@SiMS electrolyte membrane, because of the encapsulating of LiILs within the pores of SiMSs. The elimination of pores would be helpful for enhance the mechanical strength of the electrolytes (See the following Fig. 4g).

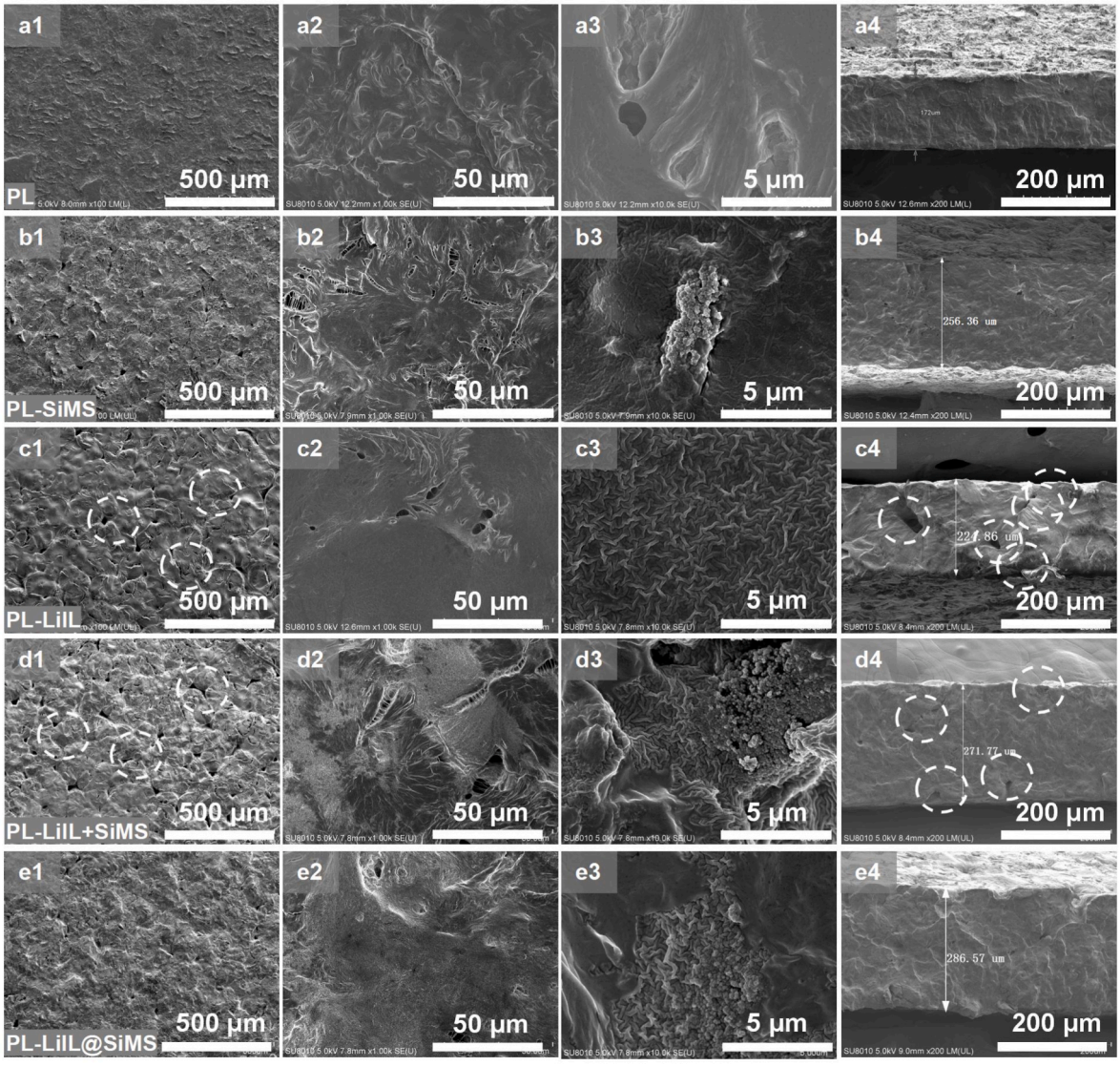


Fig. 3. SEM images of (a1-a4) PL, (b1-b4) PL-SiMS, (c1-c4) PL-LiIL, (d1-d4) PL-LiIL+SiMS, and (e1-e4) PL-LiIL@SiMS electrolytes at the surface (a1-a3, b1-b3, c1-c3, d1-d3 and e1-e3) and cross section (a4, b4, c4, d4 and e4).

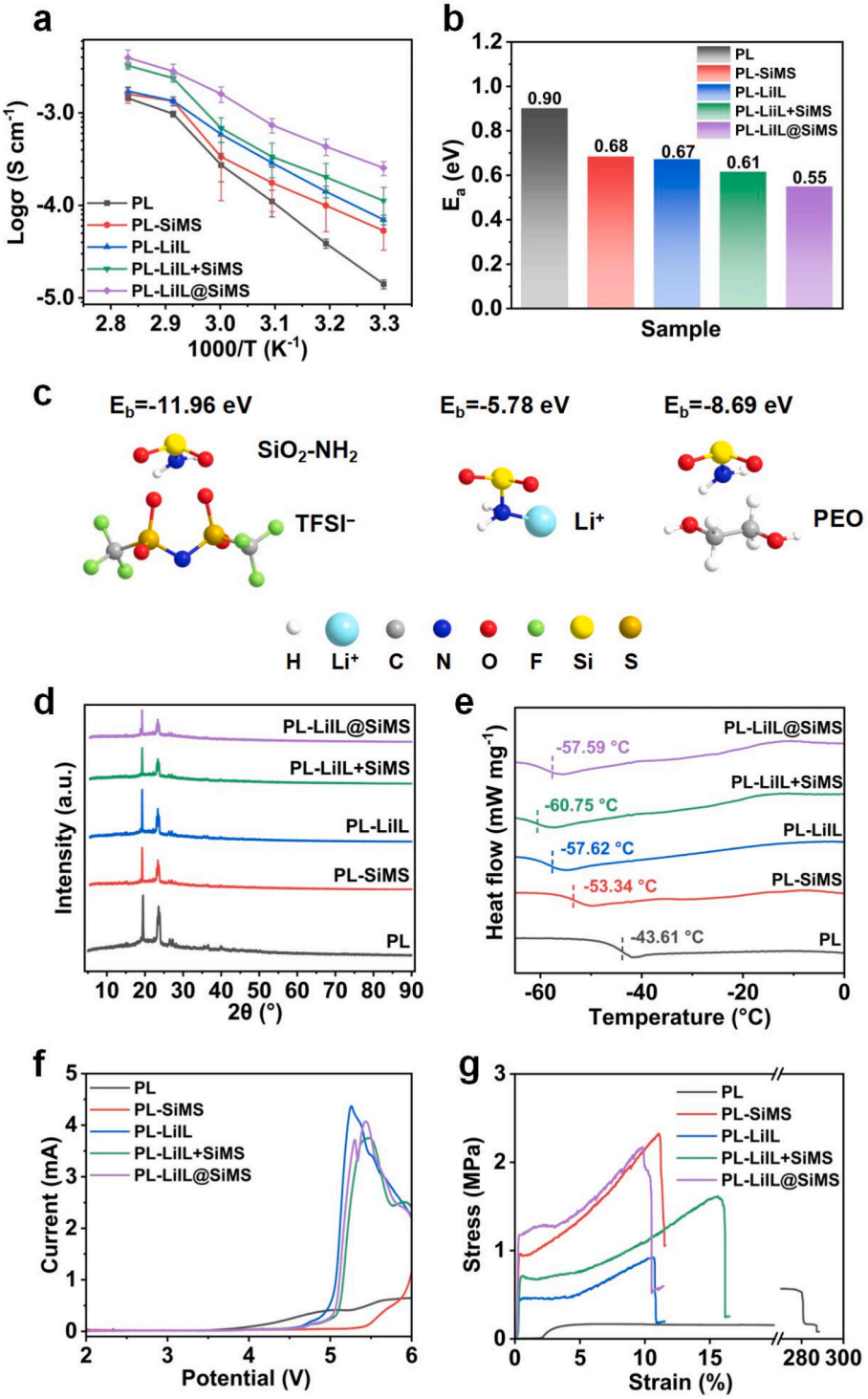


Fig. 4. (a) Arrhenius plots and (b) activation energies of PL, PL-SiMS, PL-LiIL, PL-LiIL+SiMS and PL-LiIL@SiMS electrolytes. (c) Binding energies of SiMS-$TFSI^-$, SiMS-Li^+ and SiMS-PEO pairs. (d) XRD patterns, (e) DSC curves, (f) LSV curves and (g) tensile stress-strain curves of PL, PL-SiMS, PL-LiIL, PL-LiIL+SiMS and PL-LiIL@SiMS electrolytes.

3.3. Electrical, mechanical, and thermal properties of electrolytes

Electrochemical impedance spectra were obtained for calculating the ionic conductivity of the electrolytes (Fig. S5). The pure PL electrolyte showed a low ionic conductivity of 1.41×10^{-5} S cm^{-1} at room temperature with a high E_a value of 0.90 eV (Fig. 4a–b). The incorporation of the SiMSs and LiILs resulted in the increase of the ionic conductivities to 5.32×10^{-5} and 6.99×10^{-5} S cm^{-1} for the PL-SiMS and PL-LiIL electrolytes, respectively, due to the solvation effect by the additives. Simultaneous addition of the SiMSs and LiILs led to the increase of the ionic conductivity of the PL-LiIL+SiMS electrolyte to 1.12×10^{-4} S cm^{-1}. In comparison, the PL-LiIL@SiMS electrolyte exhibited a room-temperature ionic conductivity of 2.54×10^{-4} S cm^{-1}, which was 18 times higher than that of the pure PL electrolyte. This should be attributed to the confinement of LiILs in the pores of the "particle-to-particle bridging" SiMSs and the generation of the

continuous fast-ion pathways. Meanwhile, the PL-LiIL@SiMS electrolyte showed the lowest E_a value of 0.55 eV among all the electrolytes, suggesting the fast ion transport in the PL-LiIL@SiMS electrolyte.

Surface and cross-section EDS mappings of PL-LiIL@SiMS electrolyte (Fig. S6) revealed uniform dispersion of N, O, F, Si and S elements throughout the polymer matrix, indicating that the LiIL@SiMS fillers were homogeneously distributed without significant aggregation. TEM observation (Fig. S2) showed that these fillers retained a particle-to-particle bridging morphology, which provided the structural basis for forming interconnected networks. Additionally, N_2 adsorption-desorption isotherms of SiMSs and LiIL@SiMSs (Fig. 2d–f) confirmed that the pores of SiMSs were completely filled by LiIL, transforming the insulating SiMSs into conductive building blocks. The critical role of this continuous structure was further evidenced by the significantly higher ionic conductivity of PL-LiIL@SiMS compared to PL-LiIL+SiMS, where the LiIL was simply mixed without pre-organization. Collectively, these results demonstrated that the uniformly dispersed LiIL@SiMS fillers with particle-to-particle bridging created a three-dimensional interconnected network that served as continuous fast-ion pathways, accounting for the exceptional ionic conductivity of the PL-LiIL@SiMS electrolyte.

To further evaluate the Li^+ transport characteristics, the Li^+ transference number (τ_{Li}^+) of the electrolytes was determined (Fig. S7). The PL-LiIL@SiMS electrolyte exhibits the highest τ_{Li}^+ value of 0.55, significantly higher than those of PL (0.17) and PL-SiMS (0.36). The high τ_{Li}^+ value means the effective immobilization of $TFSI^-$ and facilitation of Li^+ transport, which would effectively mitigate the concentration polarization, and contribute to the superior dendrite suppression and long-term cycling stability of Li||Li cells.

Density functional theory (DFT) calculations were performed to study the binding energies between SiMS and PEO, $TFSI^-$ and Li^+, as shown in Fig. 4c. The calculated binding energy (E_b) of SiMS-$TFSI^-$ is −11.96 eV, which is stronger than that of SiMS-Li^+ (−5.78 eV). The results indicate that SiMS can anchor $TFSI^-$ through strong hydrogen bonding interactions and promotes the dissociation of LiTFSI, leading to an increased concentration of free Li^+. The calculated binding energy of SiMS-PEO is −8.69 eV, indicating the presence of hydrogen bonding between the SiMS and PEO, which can reduce the crystallinity of PEO and improve the ionic conductivity of the electrolyte.

To unravel the underlying principles of the improved ion transfer in the composite electrolytes, XRD and DSC measurements were performed (Fig. 4d–e and S8). The pure PL electrolyte showed sharp X-ray diffraction peaks at 19° and 23°, which were corresponded to the characteristic peaks of crystalline PEO. The peak intensity greatly decreased after the addition of the LiILs and SiMSs. Especially, the PL-LiIL@SiMS electrolyte had the lowest peak intensity, indicating the greatly reduced PEO crystallinity in the composite electrolytes. DSC curves in Fig. 4e showed that the PL electrolyte showed a high glass transition temperature (T_g) of −43.61 °C. The PL-SiMS, PL-LiIL, and PL-LiIL+SiMS electrolytes showed much lower T_g values of −53.34, −57.62, and −60.75 °C, respectively, because of the solvation effect of the LiILs and SiMSs. The low T_g values also indicate the fast movement of the PEO segments, which is beneficial for increasing the ionic conductivity. It should be mentioned that the T_g value of PL-LiIL@SiMS electrolyte (−57.59 °C) was higher than that of the PL-LiIL+SiMS electrolyte, because of the confinement of the LiILs in the pores of the SiMSs, and the weakening of the solvation effect by the LiILs. Moreover, the PL-SiMS, PL-LiIL, and PL-LiIL+SiMS electrolytes had much lower PEO crystallinities of 32.0%, 23.0%, and 28.4% than the pure PL electrolyte (38.5%), respectively (Fig. S8). Similarly, the PL-LiIL@SiMS electrolyte had higher PEO crystallinity of 29.3% than the PL-LiIL+SiMS electrolyte, because of the LiIL confinement in the SiMS pores.

As shown in Fig. 4f, linear sweep voltammetry (LSV) measurements disclosed that the addition of the SiMSs and LiILs made the electrochemical oxidation stability increase from 3.88 V to 5.31 and 4.43 V, respectively. Moreover, both the PL-LiIL+SiMS and PL-LiIL@SiMS electrolytes exhibited high oxidation stability potentials of 4.65 V.

Mechanical properties of the solid electrolytes were characterized (Fig. 4g). The pure PL electrolyte showed low ultimate tensile strength of 0.60 MPa and Young's modulus of 0.21 MPa. However, the incorporation of the LiILs and SiMSs resulted in the increase of the ultimate tensile strength and Young's modulus to 0.91 and 8.30 MPa for the PL-LiIL electrolyte and 2.30 and 19.90 MPa for the PL-SiMS electrolyte, respectively. The simultaneous addition of the LiILs and SiMSs endowed the PL-LiIL+SiMS electrolyte with high tensile strength of 1.61 MPa and Young's modulus of 10.00 MPa. Because of the confinement of the LiILs in the SiMS pores, the PL-LiIL@SiMS electrolyte demonstrated higher tensile strength of 2.17 MPa and Young's modulus of 19.11 MPa than the PL-LiIL+SiMS electrolyte.

To assess the thermal stability, the electrolyte discs were subjected to isothermal exposure at different temperatures (Fig. S9). As the temperature increased from 30 to 90 °C, the shape of all the electrolyte films showed no significant change. However, when the temperature increased to 120 °C, the PL and PL-LiIL electrolytes completely melted, whereas the PL-SiMS, PL-LiIL+SiMS, and PL-LiIL@SiMS electrolytes maintained their structural integrity without shape change, due to the high thermal stability of the SiMSs additives.

3.4. Resistance against Li dendrites of electrolytes

To study the dendrite suppression effect of the electrolytes, Li||Li symmetric cells were assembled and tested at increasing current densities (Fig. 5a–c). The pure PL electrolyte-containing Li||Li cell showed a CCD value of 0.25 mA cm^{-2}. With the incorporation of high-modulus SiMSs in the PL electrolyte, the CCD value of the Li|PL-SiMS|Li and Li|PL-LiIL@SiMS|Li cells increased to 0.30 mA cm^{-2}, demonstrating effective lithium dendrite suppression capability, which should be attributed to the much high mechanical modulus of the PL-SiMS and PL-LiIL@SiMS electrolytes (Fig. 4g).

To further evaluate the durability of the electrolyte membranes during lithium stripping/deposition cycles, long-term cycling of the Li||Li symmetric cells at 0.1 mA cm^{-2} was performed (Fig. 5d–f). The Li|PL|Li cell displayed pronounced voltage oscillations peaking at 0.164 V, followed by obvious short circuiting after 616 h of operation. This failure is commonly attributed to the low ionic conductivity and insufficient mechanical strength of the PL electrolyte, causing uneven lithium deposition, dendrite formation, and penetration of the electrolyte membrane. The noticeable potential fluctuations observed in the Li||Li cell (Fig. 5d) is indicative of interfacial instability during cycling, which should be attributed to the continuous formation and rupture of the solid electrolyte interphase (SEI) layer, driven by the low mechanical strength (Young's modulus of 0.21 MPa) and insufficient ionic conductivity and Li^+ transference number of the PL electrolyte. These deficiencies led to uneven Li^+ flux distribution and local current density inhomogeneities, resulting in non-uniform Li deposition/dissolution and persistent SEI reconstruction. In comparison, though the severe voltage oscillations, the Li|PL-SiMS|Li cell possessed a longer cycling life of 4167 h, because of the improved ionic conductance and mechanical strength of the PL-SiMS electrolyte. Especially, the Li|PL-LiIL@SiMS|Li cell maintained a stable voltage plateau throughout over 6532 h at 0.10 mA cm^{-2} (Figs. 5f) and 500 h at 0.20 mA cm^{-2} of cycling (Fig. S10), demonstrating exceptional interfacial compatibility between the composite electrolyte and lithium metal electrodes.

To investigate change in resistance during the cycling process, electrochemical impedance measurements were conducted on the Li||Li symmetric cells before cycling, after 600 h of cycling, and after the completion of the long-term cycling test (Fig. 5g–i). Before cycling, the Li|PL|Li cell exhibited a much higher R_f value of 427.2 Ω compared to the Li|PL-SiMS|Li (224.0 Ω) and Li|PL-LiIL@SiMS|Li (202.1 Ω) cells, indicating that the incorporation of fillers effectively reduced the initial interfacial barrier. After 600 h of cycling, the R_f values of all the cells

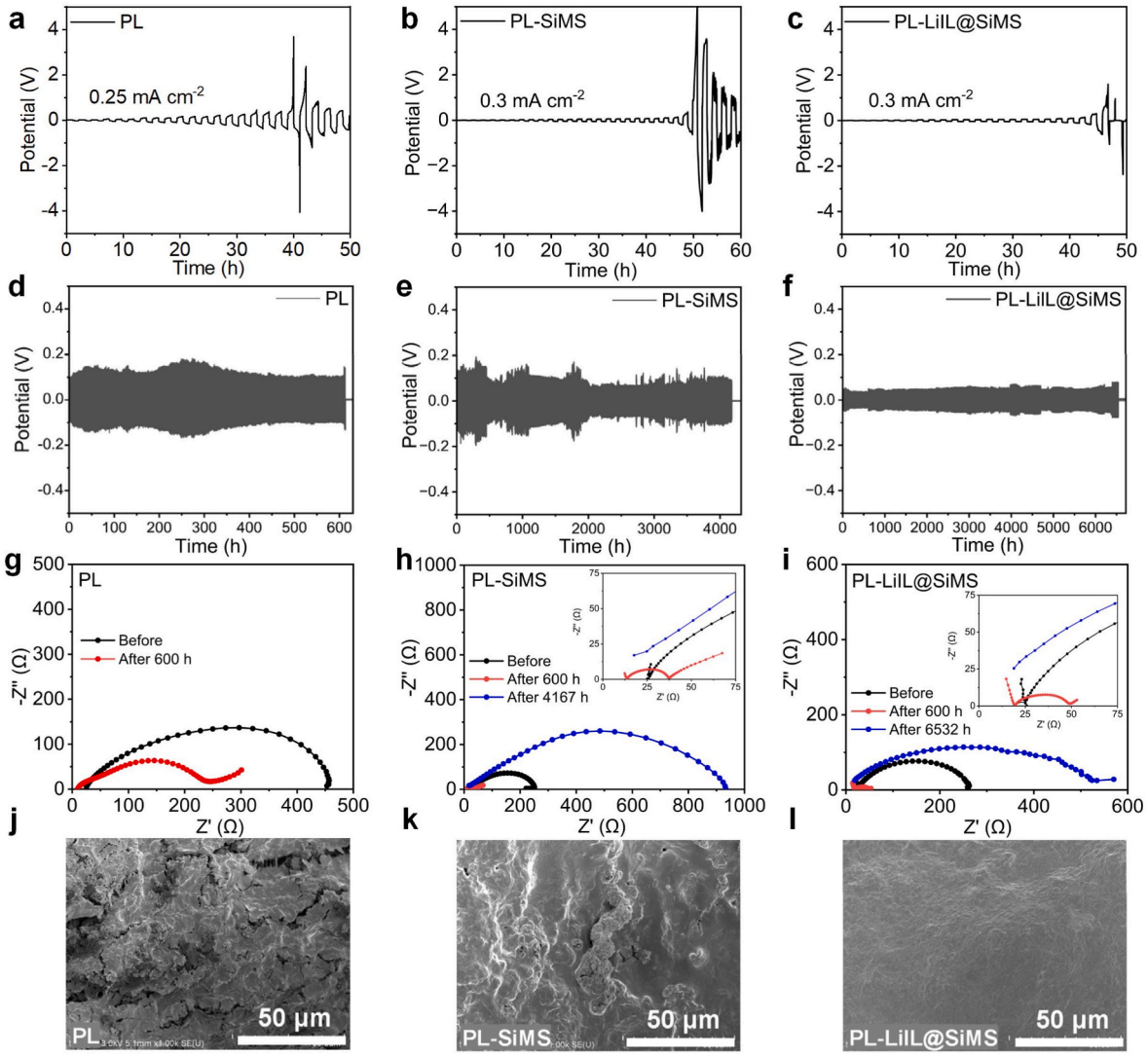


Fig. 5. Critical current density tests of (a) PL, (b) PL-SiMS and (c) PL-LiIL@SiMS electrolyte-based Li||Li cells at 60 °C. Galvanostatic cycling curves of (d) PL, (e) PL-SiMS and (f) PL-LiIL@SiMS electrolyte-based Li||Li cells at 0.10 mA cm^{-2} and 60 °C. Electrochemical impedance spectra of Li||Li cells based on (g) PL, (h) PL-SiMS and (i) PL-LiIL@SiMS electrolytes before and after Li stripping/plating processes. SEM images of the surfaces of the cycled Li electrodes paired with (j) PL, (k) PL-SiMS and (l) PL-LiIL@SiMS electrolytes.

decreased due to improved electrolyte/electrode interfacial contact, with the Li|PL-LiIL@SiMS|Li cell still showing the lowest R_f value (25.6 Ω). After the full cycling test, distinct evolution patterns emerged. The Li|PL-SiMS|Li cell exhibited a substantial R_f value increase from 224.0 Ω to 932.5 Ω after 4167 h. In contrast, the Li|PL-LiIL@SiMS|Li cell showed only a slight increase from 202.1 Ω to 541.4 Ω even after 6532 h. This stable interfacial resistance throughout the extended cycling directly explains the superior long-term cycling stability of the PL-LiIL@SiMS electrolyte.

Fig. 5j–l shows the surficial SEM images of the lithium electrodes of the cycled Li||Li cells. The lithium electrodes paired with the PL and PL-SiMS electrolytes exhibit a large number of mossy and spherical lithium dendrites, which are harmful to the long-term cycling stability of the cells. In contrast, the lithium electrodes paired with the PL-LiIL@SiMS electrolyte is smooth without obvious lithium dendrite growth, confirming the stronger lithium dendrite inhibition ability of the PL-LiIL@SiMS electrolyte. The chemical composition of the SEI layer was analyzed by XPS (Fig. S11). The C 1s spectrum of the Li electrode cycled with the PL electrolyte shows distinct $-CF_3$ and C=O peaks, indicating high organic content from incomplete decomposition, while these peaks are absent for the Li electrode paired with the PL-LiIL@SiMS electrolyte. Moreover, for the Li electrode cycled with the PL electrolyte, only a weak LiF signal is detected in the F 1s spectrum. In contrast, the Li electrode cycled with the PL-LiIL@SiMS electrolyte exhibits a strong LiF peak together with a distinct Li_3N signal in the N 1s spectrum. The LiF-rich SEI provides high mechanical strength to physically suppress dendrite growth, while the presence of Li_3N enhances Li^+ conductivity at the interface. This robust and highly conductive SEI layer is key to the exceptional interfacial compatibility and long-term cycling stability of the PL-LiIL@SiMS electrolyte-based cells.

3.5. LMB cycling performance

To evaluate the practical application of the electrolytes, solid-state Li||LFP cells were assembled and tested at 60 °C under various current densities (Fig. 6a–c, S12 and S13). The Li|PL|LFP and Li|PL-SiMS|LFP cells exhibited rapid capacity decay at 0.2–0.3C, accompanied with the irreversible capacity loss even when returning to 0.1C. In contrast, the Li|PL-LiIL@SiMS|LFP cell demonstrated superior rate performance, delivering higher discharge capacities of 175.8, 164.0, and 116.8 mAh g^{-1} at 0.1, 0.2, and 0.3C, respectively, because of the fast-ion pathways in the PL-LiIL@SiMS electrolyte. Observing the charge-discharge

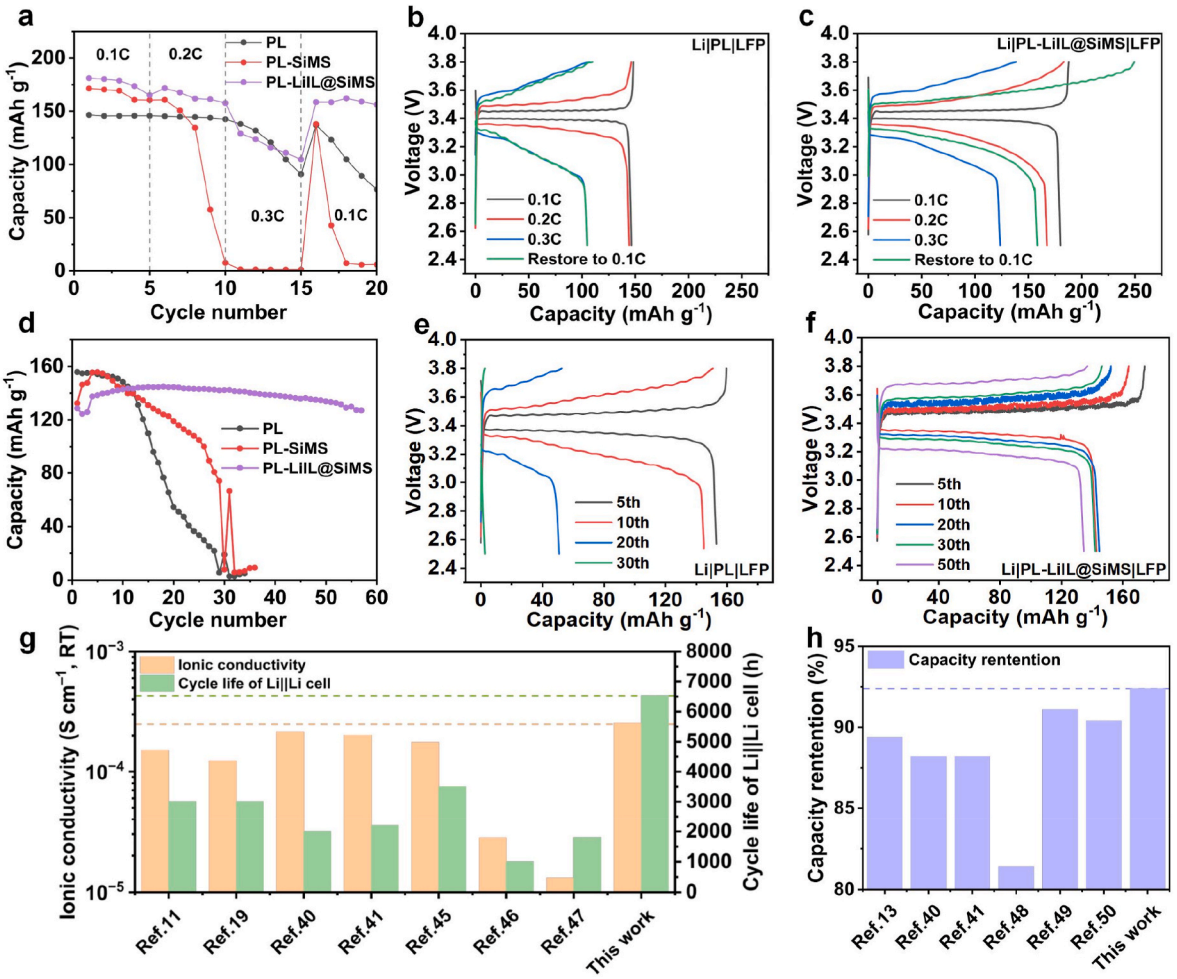


Fig. 6. (a) Rate performance of solid-state Li||LFP cells at 60 °C. Charge/discharge voltage profiles of (b) Li|PL|LFP and (c) Li|PL-LiIL@SiMS|LFP cells at various rates. (d) Cycling performance of solid-state Li||LFP cells at 60 °C and 0.1C. Charge/discharge voltage profiles of (e) Li|PL|LFP and (f) Li|PL-LiIL@SiMS|LFP cells. Comparison of (g) room-temperature ionic conductivity of electrolytes and cycle life of Li||Li cells, and (h) Li||LFP cell performance reported in open literatures [11, 13,19,40,41,45–50]. More details are given in Table S1.

voltage profiles of the Li|PL-LiIL@SiMS|LFP cell at various rates, the relatively flat plateau is observed at around 3.45 V at 0.1C in the charge process, indicating negligible electrode polarization. As the current density increases to 0.2C and 0.3C, the charge potential plateau shifts to around 3.50 and 3.55 V, respectively, because of the strengthened ohmic polarization and electrochemical polarization, while the tails at the end of the charge processes is typical characteristic of concentration polarization arising from limited Li^+ diffusion. When the rate returns to 0.1C after high-rate cycling, the charge potential plateau stabilizes at around 3.50 V with a mild slope, suggesting partial irreversible polarization accumulation, likely due to SEI evolution or interfacial degradation.

Long-term cycling stability tests of the Li||LFP batteries were conducted at 0.1C and 60 °C (Fig. 6d–f and S14). During the first three cycles, the discharge capacities of the cells increased, because of the improvement in the electrolyte/electrode interfacial contact and the activation of the LFP electrodes. Both the Li|PL|LFP and Li|PL-SiMS|LFP cells delivered rapid capacity decay. By comparison, the Li|PL-LiIL@SiMS|LFP cell exhibited exceptional cycling stability, delivering an initial discharge capacity of 137.5 mAh g^{-1} and a high capacity retention of 92.4% after 58 cycles. This is attributed to the high ionic conductivity and superior mechanical strength of the PL-LiIL@SiMS electrolyte. Furthermore, the Li|PL-LiIL@SiMS|LFP cell had an initial discharge capacity of 138.9 mAh g^{-1} at 60 °C and 0.3C (Fig. S15). After 30 cycles, the cell still maintained a capacity retention of 89.4%.

To investigate the electrochemical behavior within the Li||LFP batteries, electrochemical impedance measurements were conducted before and after the cycling process (Fig. S16). The impedance spectra were consisted of semicircles in the mid-high frequency regions and linear tails in the low-frequency regions. The ohmic resistance (R_e) and charge transfer resistance (R_{ct}) values were obtained via a Zview software by an equivalent circuit fitting. The Li|PL-LiIL@SiMS|LFP cell showed a lower R_{ct} value of 93.3 Ω than the Li|PL|LFP (99.9 Ω) and Li|PL-SiMS|LFP (142.5 Ω) cells before the cycling. Even after the cycling process, the Li|PL-LiIL@SiMS|LFP cell also showed a lower R_{ct} value of 2882.2 Ω than the Li|PL|LFP (7426.8 Ω) and Li|PL-SiMS|LFP (4309.7 Ω) cells. This explains why the Li|PL-LiIL@SiMS|LFP cell exhibited better rate performance and cycling stability. Besides, we can conclude that the capacity fading originated from the formation of SEI layers and the poor electrode/electrolyte interfacial contact during the charge-discharge processes, based on the analyses of XPS and EIS results (Fig. S11 and S16).

Table S1 presents a comparison of the electrolyte properties in this work with other existing literatures. Compared to other PEO-based solid electrolytes, the PL-LiIL@SiMS electrolyte exhibits a significantly higher room-temperature ionic conductivity (Fig. 6g). Additionally, the Li||Li cells based on the PL-LiIL@SiMS electrolyte demonstrate exceptional long-term cycling stability. The cycling performance of the Li|PL-LiIL@SiMS|LFP (Fig. 6h) and Li|PL-LiIL@SiMS|$LiNi_{0.6}Co_{0.2}Mn_{0.2}O_2$ (Fig. S17) cells further confirms the application potentials in high-voltage LMBs.

4. Conclusions

In summary, a multifunctional LiIL@SiMS filler was exploited to comprehensively improve PEO-based electrolytes. Because of the formation of continuous fast-ion pathways within the SiMSs with "particle-to-particle bridging" networks, the ambient-temperature ionic conductivity increased by 18 times to 2.54×10^{-4} S cm^{-1} for the PL-LiIL@SiMS electrolyte. The electrochemical oxidation stability potential and mechanical strength also increased from 3.88 V and 0.60 MPa to 4.65 V and 2.17 MPa, respectively, due to the confinement of LiILs in the SiMSs and the 3D continuous LiIL@SiMS arrangement in the electrolyte. Consequently, the Li|PL-LiIL@SiMS|Li cell showed much longer cycling life of 6532 h than the Li|PL|Li cell (616 h). Furthermore, the PL-LiIL@SiMS electrolyte-based LMBs exhibited better rate performance and cycling stability, showing great application prospect.

CRediT authorship contribution statement

Lehao Liu: Conceptualization, Data curation, Formal analysis, Funding acquisition, Investigation, Methodology, Project administration, Resources, Software, Validation, Visualization, Writing – original draft, Writing – review & editing. **Baoyi Wang:** Conceptualization, Data curation, Formal analysis, Funding acquisition, Investigation, Methodology, Project administration, Resources, Software, Validation, Visualization, Writing – original draft, Writing – review & editing. **Mengxuan Zhang:** Conceptualization, Data curation, Formal analysis, Funding acquisition, Investigation, Methodology, Project administration, Resources, Software, Validation, Visualization, Writing – original draft, Writing – review & editing. **Kunda Yang:** Data curation, Formal analysis, Software, Writing – original draft. **Dingrong Long:** Data curation, Formal analysis, Software, Writing – original draft. **Dongmei Zhang:** Data curation, Formal analysis, Software, Writing – original draft. **Rubing Xu:** Data curation, Formal analysis, Software, Writing – original draft. **Jiaxin Tu:** Data curation, Formal analysis, Software, Writing – original draft. **Jiangping Zhang:** Data curation, Formal analysis, Software, Writing – original draft. **Wei Lv:** Formal analysis, Investigation, Methodology, Software, Validation, Visualization, Writing – review & editing. **Shigang Ling:** Formal analysis, Investigation, Methodology, Software, Validation, Visualization, Writing – review & editing. **Jianan Gu:** Formal analysis, Investigation, Methodology, Software, Validation, Visualization, Writing – review & editing. **Lihua Chu:** Formal analysis, Investigation, Methodology, Software, Validation, Visualization, Writing – review & editing. **Bing Jiang:** Formal analysis, Investigation, Methodology, Software, Validation, Visualization, Writing – review & editing. **Qianxiao Fan:** Formal analysis, Investigation, Methodology, Software, Validation, Visualization, Writing – review & editing. **Ziyue Wen:** Formal analysis, Investigation, Methodology, Software, Validation, Visualization, Writing – review & editing. **Meicheng Li:** Conceptualization, Funding acquisition, Investigation, Methodology, Project administration, Supervision.

Declaration of competing interest

The authors declare that they have no known competing financial interests or personal relationships that could have appeared to influence the work reported in this paper.

Acknowledgements

This work is supported partially by project of National Natural Science Foundation of China (52272200), Beijing Natural Science Foundation (26JL001), Hebei Natural Science Foundation (E2022502022), State Key Laboratory of Alternate Electrical Power System with Renewable Energy Sources (LAPS26007),the project of China Three Gorges Corporation named key technologies of intelligent joint regulation and operation with grid connected friendly in power station group of wind, solar photovoltaic and energy storage (WWKY-2021-0173), Huaneng Group Headquarters Science and Technology Project (HNKJ20-H88), the Fundamental Research Funds for the Central University (2025MS040), and the NCEPU "Double First-Class" Program. The authors acknowledge the technology assistance of NCEPU Instrumental Analysis Center for the sample characterizations and analyses.

Appendix A. Supplementary data

Supplementary data to this article can be found online at https://doi.org/10.1016/j.jpowsour.2026.240315.

Data availability

Data will be made available on request.

References

[1] R. Che, S. Cheng, C. Huang, M. Liu, Z. Chen, J. Han, W. Chen, P. Zhang, Poly (vinylidene fluoride)-based janus separators with an ultrathin conductive layer for suppressing lithium dendrite growth, Chem. Eng. J. 509 (2025) 161238, https://doi.org/10.1016/j.cej.2025.161238.

[2] Q. Kang, Z. Zhuang, Y. Liu, Z. Liu, Y. Li, B. Sun, F. Pei, H. Zhu, H. Li, P. Li, Engineering the structural uniformity of gel polymer electrolytes via pattern-guided alignment for durable, safe solid-state lithium metal batteries, Adv. Mater. 35 (2023) 2303460, https://doi.org/10.1002/adma.202303460.

[3] X. Zhao, H. Shang, J. Ji, C. Zhu, R. Wen, G. Qi, F. Cai, Regulating interfaces of composite polymer electrolyte via surface charge on fillers for stable solid-state lithium battery, Ceram. Int. 50 (2024) 22608–22617, https://doi.org/10.1016/j.ceramint.2024.03.362.

[4] Z. Gao, H. Sun, L. Fu, F. Ye, Y. Zhang, W. Luo, Y. Huang, Promises, challenges, and recent progress of inorganic solid-state electrolytes for all-solid-state lithium batteries, Advanced materials 30 (2018) 1705702, https://doi.org/10.1002/adma.201705702.

[5] X. Tian, Y. Liu, C. Zhao, C. Li, X. Yang, J. Zhang, J. Lang, D.G. Shchukin, H. Du, M. Li, A shear-thickening fluid based on ionic liquid as dual-safe electrolyte for lithium batteries, Chem. Eng. J. 503 (2025) 158145, https://doi.org/10.1016/j.cej.2024.158145.

[6] W. Liu, S.W. Lee, D. Lin, F. Shi, S. Wang, A.D. Sendek, Y. Cui, Enhancing ionic conductivity in composite polymer electrolytes with well-aligned ceramic nanowires, Nat. Energy 2 (2017) 1–7, https://doi.org/10.1038/nenergy.2017.35.

[7] Y. Ren, S. Chen, M. Odziomek, J. Guo, P. Xu, H. Xie, Z. Tian, M. Antonietti, T. Liu, Mixing functionality in polymer electrolytes: a new horizon for achieving high-performance all-solid-state lithium metal batteries, Angew. Chem. Int. Ed. (2025) e202422169, https://doi.org/10.1002/anie.202422169.

[8] D. Zhang, X. Meng, W. Zhang, J. Mo, Q. Zhao, B. Wang, Q. Fan, L. Liu, T. Yang, Y. Jin, A thin and ultrahigh-ionic-conductivity composite electrolyte with 3D aramid nanofiber networks toward ambient-temperature lithium metal batteries, Adv. Energy Mater. 15 (2025) 2403565, https://doi.org/10.1002/aenm.202403565.

[9] H. Liu, Y. Liao, C. Leung, Y. Zhang, Y. Yang, F. Liu, Y. Wei, C. Fan, S. Zhang, D. Wang, J. Yan, Q. Liu, C. Chung, Y. Ren, Y. Huang, J. Yang, Ring-opening polymerization reconfigures polyacrylonitrile network for ultra stable solid-state lithium metal batteries, Adv. Energy Mater. 15 (2024) 2402795, https://doi.org/10.1002/aenm.202402795.

[10] D. Zhang, D. Long, J. Zhang, J. Tu, R. Xu, K. Yang, Q. Fan, W. Zhang, L. Liu, M. Li, Ultrathin composite electrolyte with multifunctional skeleton for solid-state lithium metal batteries, J. Power Sources 659 (2025) 238312, https://doi.org/10.1016/j.jpowsour.2025.238312.

[11] S. Cai, X. Du, X. Gao, C. Zhao, C. Cheng, R. Lin, X. Yang, D. Luo, R. Sun, Z. Chen, Polyoxometalate-integrated host-guest recognition solid polymer electrolytes for wide-temperature range solid-state lithium metal batteries, Nano Energy 140 (2025) 111031, https://doi.org/10.1016/j.nanoen.2025.111031.

[12] J. Guo, H. Xu, Y. Sun, K. Chen, X. Zhang, H. Xie, Y. Jiang, J. Liu, Borate-containing triblock copolymer electrolytes for improved lithium-ion transference number and interface stability, J. Colloid Interface Sci. 660 (2024) 565–573, https://doi.org/10.1016/j.jcis.2024.01.097.

[13] X. Meng, D. Zhang, J. Mo, L. Liu, T. Yang, Q. Fan, Q. Zhao, R. Zhou, M. Zhang, W. Hou, Room-temperature solid-state metallic lithium batteries based on high-content boron nitride nanosheet-modified polymer electrolytes, Appl. Surf. Sci. 648 (2024) 158962, https://doi.org/10.1016/j.apsusc.2023.158962.

[14] R. Fang, B. Xu, N.S. Grundish, Y. Xia, Y. Li, C. Lu, Y. Liu, N. Wu, J.B. Goodenough, Li_2S_6-integrated PEO-based polymer electrolytes for all-solid-state lithium-metal batteries, Angew. Chem. 133 (2021) 17842–17847, https://doi.org/10.1002/ange.202106039.

[15] K. Mu, W. Dong, W. Xu, Z. Song, R. Wang, L. Wu, H. Li, Q. Liu, C. Zhu, J. Xu, In situ hybrid crosslinking polymerization of nanoparticles for composite polymer electrolytes to achieve highly-stable solid lithium-metal batteries, Adv. Funct. Mater. 34 (2024) 2405969, https://doi.org/10.1002/adfm.202405969.

[16] H. An, M. Li, Q. Liu, Y. Song, J. Liu, Z. Yu, X. Liu, B. Deng, J. Wang, Strong Lewis-acid coordinated PEO electrolyte achieves 4.8 V-class all-solid-state batteries over

580 Wh kg^{-1}, Nat. Commun. 15 (2024) 9150, https://doi.org/10.1038/s41467-024-53094-8.
[17] C. Wang, Y. Yang, X. Liu, H. Zhong, H. Xu, Z. Xu, H. Shao, F. Ding, Suppression of lithium dendrite formation by using LAGP-PEO(LiTFSI) composite solid electrolyte and lithium metal anode modified by PEO(LiTFSI) in all-solid-state lithium batteries, ACS Appl. Mater. Interfaces 9 (2017) 13694–13702, https://doi.org/10.1021/acsami.7b00336.
[18] E.M. Masoud, A.-A. El-Bellihi, W. Bayoumy, M. Mousa, Organic-inorganic composite polymer electrolyte based on PEO-$LiClO_4$ and nano-Al_2O_3 filler for lithium polymer batteries: dielectric and transport properties, J. Alloys Compd. 575 (2013) 223–228, https://doi.org/10.1016/j.jallcom.2013.04.054.
[19] D. Hu, H. Huang, C. Wang, Q. Hong, H. Wang, S. Tang, H. Zhang, J. Li, L. Hu, L. Jiang, Tailoring multiple interactions in poly (urethane-urea)-based solid-state polymer electrolytes for long-term cycling lithium metal batteries, Adv. Energy Mater. 15 (2025) 2406176, https://doi.org/10.1002/aenm.202406176.
[20] K. Chen, J. Liu, X. Zhang, Y. Sun, H. Xie, Three-dimensional cross-linked network deep eutectic gel polymer electrolyte with the self-healing ability enable by hydrogen bonds and dynamic disulfide bonds, J. Colloid Interface Sci. 669 (2024) 529–536, https://doi.org/10.1016/j.jcis.2024.05.015.
[21] J. Li, L. Yang, H. Zhang, X. Ji, Self-healing composite solid electrolytes with enhanced Li^+ transport and mechanical properties for safe lithium metal batteries, Chem. Eng. J. 438 (2022) 135418, https://doi.org/10.1016/j.cej.2022.135418.
[22] E. Zhao, Y. Guo, Y. Liu, S. Liu, G. Xu, Nanostructured zeolitic imidazolate framework-67 reinforced poly (ethylene oxide) composite electrolytes for all solid state lithium ion batteries, Appl. Surf. Sci. 573 (2022) 151489, https://doi.org/10.1016/j.apsusc.2021.151489.
[23] C. Xue, X. Zhang, S. Wang, L. Li, C.-W. Nan, Organic-organic composite electrolyte enables ultralong cycle life in solid-state lithium metal batteries, ACS Appl. Mater. Interfaces 12 (2020) 24837–24844, https://doi.org/10.1021/acsami.0c05643.
[24] X. Zhang, J. He, Y. Sun, H. Xie, J. Liu, Enhanced inorganic-organic interphase compatibility in composite solid electrolytes by forming isocyanate-linked hybrid cross-linked networks, J. Colloid Interface Sci. (2025) 138441, https://doi.org/10.1016/j.jcis.2025.138441.
[25] Y. Sun, M. Wang, X. Zhang, H. Xie, J. Liu, Additive-free nitrile-based gel polymer electrolytes with enhanced interfacial compatibility for lithium metal batteries, Chem. Eng. J. 519 (2025) 165528, https://doi.org/10.1016/j.cej.2025.165528.
[26] L. Liu, R. Xu, J. Tu, R. Zhou, J. Mo, T. Yang, Q. Zhao, M. Zhang, D. Zhang, M. Li, Thin polymer electrolytes with 3D nanofiber skeletons enabling high-performance solid-state lithium metal batteries, J. Phys. Chem. C 129 (2025) 6138–6147, https://doi.org/10.1021/acs.jpcc.5c00814.
[27] J. Hu, W. Wang, X. Zhu, S. Liu, Y. Wang, Y. Xu, S. Zhou, X. He, Z. Xue, Composite polymer electrolytes reinforced by hollow silica nanotubes for lithium metal batteries, J. Membr. Sci. 618 (2021) 118697, https://doi.org/10.1016/j.memsci.2020.118697.
[28] J. Wu, X. Zuo, Q. Chen, X. Deng, H. Liang, T. Zhu, J. Liu, W. Li, J. Nan, Functional composite polymer electrolytes with imidazole modified SiO_2 nanoparticles for high-voltage cathode lithium ion batteries, Electrochim. Acta 320 (2019) 134567, https://doi.org/10.1016/j.electacta.2019.134567.
[29] Y. Cheng, Z. Cai, J. Xu, Z. Sun, X. Wu, J. Han, Y.H. Wang, M.S. Wang, Zwitterionic cellulose-based polymer electrolyte enabled by aqueous solution casting for high-performance solid-state batteries, Angew. Chem. Int. Ed. 63 (2024) e202400477, https://doi.org/10.1002/anie.202400477.
[30] Z. Lei, J. Shen, J. Wang, Q. Qiu, G. Zhang, S.-S. Chi, H. Xu, S. Li, W. Zhang, Y. Zhao, Composite polymer electrolytes with uniform distribution of ionic liquid-grafted ZIF-90 nanofillers for high-performance solid-state Li batteries, Chem. Eng. J. 412 (2021) 128733, https://doi.org/10.1016/j.cej.2021.128733.
[31] L. Liu, J. Mo, R. Zhou, T. Yang, R. Xu, J. Tu, Q. Zhao, M. Zhang, D. Zhang, B. Wang, D. Long, K. Yang, J. Zhang, M. Li, Ultrathin solid composite electrolytes for long-life lithium metal batteries, J. Energy Storage 114 (2025) 115777, https://doi.org/10.1016/j.est.2025.115777.
[32] C. Han, H. Shen, M. Li, Y. Tian, Y. Chen, X. Wu, J. Sun, L. Liu, X. Zhang, J. Tang, Nano-confined synergistic conduction enables electrolytes for all-solid-state lithium metal batteries, Adv. Funct. Mater. (2025) e23139, https://doi.org/10.1002/adfm.202523139.
[33] V. Vijayakumar, M. Ghosh, K. Asokan, S.B. Sukumaran, S. Kurungot, J. Mindemark, D. Brandell, M. Winter, J.R. Nair, 2D layered nanomaterials as fillers in polymer composite electrolytes for lithium batteries, Adv. Energy Mater. 13 (2023) 2203326, https://doi.org/10.1002/aenm.202203326.
[34] Y. Jiang, K. Chen, J. He, Y. Sun, X. Zhang, X. Yang, H. Xie, J. Liu, A self-healing composite solid electrolyte with dynamic three-dimensional inorganic/organic hybrid network for flexible all-solid-state lithium metal batteries, J. Colloid Interface Sci. 678 (2025) 200–209, https://doi.org/10.1016/j.jcis.2024.09.119.
[35] R. Zhao, Y. Wu, Z. Liang, L. Gao, W. Xia, Y. Zhao, R. Zou, Metal-organic frameworks for solid-state electrolytes, Energy Environ. Sci. 13 (2020) 2386–2403, https://doi.org/10.1039/D0EE00153H.
[36] X. Chi, M. Li, J. Di, P. Bai, L. Song, X. Wang, F. Li, S. Liang, J. Xu, J. Yu, A highly stable and flexible zeolite electrolyte solid-state Li-air battery, Nature 592 (2021) 551–557, https://doi.org/10.1038/s41586-021-03410-9.
[37] S. Liang, K. Qian, M. Xu, W. Cui, Y. Li, Y. Lu, S. Liu, S. Zhao, Z. Xue, C. Guo, Fiber-architected solid polymer electrolytes: multiscale engineering, scalable fabrication, and operando characterization for high-conductivity solid-state batteries, J. Alloys Compd. 1033 (2025) 181297, https://doi.org/10.1016/j.jallcom.2025.181297.
[38] L. Liu, T. Yang, R. Xu, D. Long, J. Tu, R. Zhou, Q. Zhao, M. Li, Hydrogen bond interaction enhanced polymer electrolytes through functionalized nanosheets for high-stability lithium metal batteries, Appl. Surf. Sci. 717 (2026) 164825, https://doi.org/10.1016/j.apsusc.2025.164825.
[39] H. Wu, S. Jian, S. Xue, Z. Ma, C. Li, S. Deng, W. Feng, Y. Cao, Q. Dou, L. Yang, Synergistic ion transport facilitated by one-dimension wollastonite in solid polymer electrolytes for stable lithium metal batteries, J. Power Sources 584 (2023) 233613, https://doi.org/10.1016/j.jpowsour.2023.233613.
[40] X. Gao, Z. Zheng, Y. Pan, S. Song, Z. Xu, Aligned hollow silicon nanorods containing ionic liquid enhanced solid polymer electrolytes with superior cycling and rate performance, Adv. Sci. 12 (2025) 2411437, https://doi.org/10.1002/advs.202411437.
[41] H. Lian, X. Hu, D. Xiong, S. Tao, B. Zhong, B. Song, W. Deng, H. Hou, G. Zou, X. Ji, Local charge redistribution enables single ionic conductor for fast charge solid Li battery, Energy Storage Mater. 71 (2024) 103593, https://doi.org/10.1016/j.ensm.2024.103593.
[42] Z. Wang, R. Tan, H. Wang, L. Yang, J. Hu, H. Chen, F. Pan, A metal-organic-framework-based electrolyte with nanowetted interfaces for high-energy-density solid-state lithium battery, Adv. Mater. 30 (2018) 1704436, https://doi.org/10.1002/adma.201704436.
[43] X. Tang, S. Lv, K. Jiang, G. Zhou, X. Liu, Recent development of ionic liquid-based electrolytes in lithium-ion batteries, J. Power Sources 542 (2022) 231792, https://doi.org/10.1016/j.jpowsour.2022.231792.
[44] L. Liu, T. Yang, R. Zhou, R. Xu, J. Tu, Q. Zhao, D. Long, M. Li, Comprehensively-upgraded polymer electrolytes with lithium ion-conductive nanosheets towards stable lithium metal batteries, Chem. Eng. J. 521 (2025) 166963, https://doi.org/10.1016/j.cej.2025.166963.
[45] T. Duan, J. Li, L. Li, Q. Sun, X. Lu, H. Cheng, An oxygen-defective framework with intensified lewis acidity reinforcing composite electrolyte for all-solid-state lithium metal batteries, Energy Storage Mater. 73 (2024) 103847, https://doi.org/10.1016/j.ensm.2024.103847.
[46] A. Du, H. Lu, S. Liu, S. Chen, Z. Chen, W. Li, J. Song, Q.H. Yang, C. Yang, Breaking the trade-off between ionic conductivity and mechanical strength in solid polymer electrolytes for high-performance solid lithium batteries, Adv. Energy Mater. 14 (2024) 2400808, https://doi.org/10.1002/aenm.202400808.
[47] Q. Song, Y. Zhang, J. Liang, S. Liu, J. Zhu, X. Yan, Boron nitride nanofibers enhanced composite PEO-based solid-state polymer electrolytes for lithium metal batteries, Chin. Chem. Lett. 35 (2024) 108797, https://doi.org/10.1016/j.cclet.2023.108797.
[48] T.I. Kolesnikov, D. Voll, F. Jeschull, P. Theato, Synthesis of Polyimide-PEO copolymers: toward thermally stable solid polymer electrolytes for lithium-metal batteries, Eur. Polym. J. 217 (2024) 113315, https://doi.org/10.1016/j.eurpolymj.2024.113315.
[49] L. Bertoli, G. Gabriele, E. Gibertini, L. Magagnin, Unconventional PEO-PPC quasi-solid state blend polymer electrolyte for high efficiency solid-state Li-metal batteries, J. Energy Storage 81 (2024) 110456, https://doi.org/10.1016/j.est.2024.110456.
[50] Y. He, J. Guo, C. Bi, Z. Hao, C. Li, Q. Wang, X. Han, Sandwich-like polyimide nanofiber membrane of PEO-based solid-state electrolytes to promote mechanical properties and security for lithium metal batteries, Int. J. Hydrogen Energy 109 (2025) 1266–1273, https://doi.org/10.1016/j.ijhydene.2025.02.086.